EUROPEAN ORGANIZATION FOR NUCLEAR RESEARCH

CERN-EP/84-46
10 April 1984

JETS IN HIGH TRANSVERSE ENERGY EVENTS AT THE CERN INTERSECTING STORAGE RINGS

CERN[1]-Michigan State[2]-Oxford[3]-Rockefeller[4] (CMOR) Collaboration

A.L.S. Angelis[3], G. Basini[1,*], H.-J. Besch[1], R.E. Breedon[4], L. Camilleri[1], T.J. Chapin[4], R.L. Cool[4], P.T. Cox[1,4], C. von Gagern[1,4], C. Grosso-Pilcher[1,**], D.S. Hanna[1,4,***], B.M. Humphries[2], J.T. Linnemann[4], C.B. Newman-Holmes[1,†], R.B. Nickerson[3,††], N. Phinney[1,3,†††], B.G. Pope[2], S.H. Pordes[1,4,†], K.J. Powell[3], R.W. Rusack[4], C.W. Salgado[2], A.M. Segar[3], S.R. Stampke[2], M.J. Tannenbaum[4,#] and J.M. Yelton[3,†††]

ABSTRACT

Most events with high neutral transverse energy, E^{o}_{T}, produced in pp collisions at $\sqrt{s}$ = 62.3 GeV, are jet-like. The evidence for this is presented, based on data collected using an electromagnetic calorimeter covering 90% of 2π in azimuth. The spectrum dN/dE^{o}_{T} has been measured over the E^{o}_{T} range from 10 to 35 GeV. Properties of the observed jets are discussed.

(Submitted to Nuclear Physics B)

---

1) CERN, Geneva, Switzerland
2) Michigan State University, East Lansing, MI, USA
3) Oxford University, Oxford, England
4) Rockefeller University, New York, NY, USA

*) Present address: Laboratori Nazionali dell' INFN, Frascati, Italy
**) Present address: Enrico Fermi Institute, University of Chicago, Chicago, IL, USA
***) Present address: National Research Council, Ottawa, Ontario, Canada
†) Present address: FNAL, Batavia, IL, USA
††) Present address: Lyman Laboratory of Physics, Harvard University, Cambridge, MA, USA
†††) Present address: SLAC, Stanford, CA, USA
#) Present address: BNL, Upton, NY, USA

1. INTRODUCTION

There is now considerable evidence for a large amount of jet production in hadron-hadron collisions at high transverse energies even when the trigger places little geometrical constraint on the events, at centre of mass (c.m.) energies ranging from the CERN Intersecting Storage Rings (ISR) ($\sqrt{s}$ = 62 GeV)[1,2] to the Super Proton Synchrotron (SPS) Collider ($\sqrt{s}$ = 540 GeV) [3]. This does not appear to be the case at lower energies ($\sqrt{s}$ = 24 GeV) [4]. The increasing dominance of two-jet production with increasing transverse energy in the ISR energy range ($\sqrt{s}$ = 62.3 GeV) was first shown in ref. 1 for events triggered on an electromagnetic calorimeter covering 90% of 2π in azimuth. This paper extends and develops the work reported in ref. 1, and examines some properties of the jets observed.

2. APPARATUS

The apparatus, shown in fig. 1, consisted of a superconducting solenoid providing a 1.4 T magnetic field surrounding a set of concentric cylindrical drift chambers, DCM1—5. The electromagnetic calorimeter comprised four modules of lead/scintillator shower counters inside the solenoid, and two modules of lead glass outside the magnet in the azimuthal region not covered by the shower counters. The electromagnetic calorimeter's acceptance in the proton-proton c.m. system is depicted in fig. 2.

Each shower counter module was 1.5 m long, and subtended 50° in azimuth and ±1.1 units of rapidity y, centred on y = 0, and was segmented azimuthally into eight counters. Each counter was 14 radiation lengths (RL) thick, and consisted of 16 layers of scintillator interleaved with layers of lead. The 4 layers nearest the beam interaction region ("front"), and the remaining 12 layers ("back") were independently viewed by phototubes at each end of the counter. Each lead-glass module consisted of a front array of 34 blocks, each 4 RL thick, and a back array of 168 blocks, each 17 RL thick, all of type SF5 lead glass. The angular acceptance of each lead-glass array was ±0.6 units of rapidity, also centred on y = 0, and in azimuth 57° for the back arrays and 45° for the front arrays. Both the shower counters and lead glass were initially calibrated in an electron beam at the CERN Proton Synchrotron. Subsequently, the calibration of the shower counters and front lead glass was monitored using a system of light flashers (krytrons) connected to the counters and a set of reference counters by fibre optics. The stability of the krytron light output was monitored by comparison in a reference counter with the light output from a NaI crystal on which was mounted a ^{137}Cs source. The calibration of the back glass [5] was monitored with NaI crystals doped with ^{241}Am. All the electromagnetic counters were also monitored using minimum ionizing particles, mainly cosmic-ray initiated

muons. The r.m.s. energy resolution of the lead glass was $(4.3/\sqrt{E} + 2)\%$, and that of the shower counters was $(16/\sqrt{E})\%$, with E in GeV.

Charged particles were measured over the full azimuth, and in the rapidity range ±1.2 centred on $y = 0$, using the drift chambers. The spatial resolution was about 350 μm, yielding a momentum resolution of $\Delta p_T/p_T = (7\%)p_T$ with p_T in GeV/c. Further details of the solenoid and the drift chambers are available elsewhere [6].

Finally, there were two hodoscopes of scintillation counters, a barrel hodoscope (A) consisting of 32 azimuthal counters located between the innermost and neighbouring drift-chamber modules, and a hodoscope (B) of 24 azimuthal counters located outside the solenoid, 12 in front of each lead-glass module. Each of these scintillation counters was equipped with a phototube at each end.

3. EVENT SELECTION

The apparatus was triggered when the sum of all energies deposited in the shower counters and lead-glass counters was greater than some predetermined threshold. In the off-line analysis this energy threshold was applied again, after correcting the observed pulse heights using more detailed calibration information.

The trigger placed little requirement on the pattern of energy deposition, so the high instantaneous luminosity at the ISR (typically 6×10^{31} $cm^{-2}s^{-1}$ for these data) meant that most events were due to the overlap of more than one interaction, each with energy below the threshold, occurring during the recording time of the apparatus. Such spurious events were identified by examining the times of the counter hits in the events. Each phototube signal from all shower counters was split so that it could be fed into the trigger logic, into an analog-to-digital converter (ADC) for pulse-height information, and into a time-to-digital converter (TDC) for time information. The phototube signals from the A scintillators surrounding the interaction region were fed into TDCs capable of recording up to 14 hits per counter end in a time interval from 300 ns before to 300 ns after the nominal event time. The time data from the shower counters and the A scintillators were searched in a range ±200 ns (the longest gate time used in the calorimeter) relative to the nominal event time. A time cluster was defined as two or more counter hits occurring within a 12 ns interval. If more than one distinct cluster was found the event was rejected. This procedure was verified by checking the consistency of multiple time clusters found in different counter systems, by the tendency for there to be double vertices in the charged tracks when close multiple time clusters were found, and by examining the effect of the cuts on data collected at several different instan-

taneous luminosities. The raw event rate was a strong function of the instantaneous luminosity, but after the time cluster cuts this dependence was removed, and both raw and cut event rates extrapolated to the same point at zero instantaneous luminosity [1].

Each event was required to contain at least two charged tracks, with two or more of these tracks intersecting at a point, the vertex, well within the pp interaction region. In addition, it was required that there was some energy-sharing between the front and back compartments of all six electromagnetic calorimeter modules, in order to remove a small contamination of the event sample by interactions due to cosmic rays and stray beam protons.

4. NEUTRAL TRANSVERSE ENERGY SPECTRUM

A shower counter or lead-glass block was considered to be hit if it contained energy above a noise threshold of 70 MeV or 15 MeV respectively. In each shower counter the longitudinal (along the colliding-beam axis) position of energy deposition was calculated from the time difference or energy difference between the phototube signals at each end. From each hit a momentum vector was constructed, assuming the hit was caused by a massless neutral particle emerging from the event vertex. Each momentum vector was Lorentz transformed from the laboratory system to the c.m. system of the colliding protons, and the transverse energy in the pp c.m. calculated as $|p_T|$. The sum of these energies gave the total transverse neutral energy E^0_T. The spectrum $(1/\mathscr{L})(dN/dE^0_T)$, shown in fig. 3, was obtained by dividing the number of events per GeV of E^0_T by the integrated luminosity, $\mathscr{L} = 2.875 \times 10^{37}$ cm^{-2}. To cover the E^0_T range 1 to 35 GeV, five trigger thresholds were used: 1, 10, 15, 20, and 25 GeV, with 94% of the integrated luminosity accumulated at the highest threshold. The data from all thresholds merged smoothly into each other and they have been combined in fig. 3. The spectrum deviates from a simple exponential above E^0_T of 20 GeV, as was already reported in ref. 1. A deviation from purely exponential behaviour of the E_T spectrum at $\sqrt{s}$ = 540 GeV has also been seen by the UA2 Collaboration [7]. The result of a fit to an exponential in E^0_T over the range 10 to 20 GeV is shown [$\sim\exp(-0.93E^0_T)$]. No corrections have been made for resolution, double hits in the same shower counter, or energy deposited by charged tracks in the electromagnetic calorimeter. These corrections are not expected to be large, but will tend to increase the slope of the spectrum by at most 20%. The deviation from exponential behaviour will be further discussed in section 6.3.

5. TRANSVERSE ENERGY IN CHARGED PARTICLES

The transverse energy of the charged particles, E^c_T, in the event was obtained from the tracks measured in the drift chambers. Only charged tracks of $p_T > 300$ MeV/c were considered (reconstruction of lower momentum tracks drastically increased the amount of computing time required), and tracks not pointing to the event vertex were discarded. Figure 4a shows the mean value of the ratio E^c_T/E^o_T as a function of E^o_T. The smallness of these values, and the decrease with increasing E^o_T from 0.6 to 0.2, is due to triggering on only the electromagnetic part of the total event energy. In fig. 4b the mean value of E^c_T is shown to be almost independent of E^o_T, with a value of about 7 GeV. This could be an underestimate by as much as 3 GeV, due to the stringent vertex requirement.

6. THE EVIDENCE FOR JET DOMINANCE

The structure of the events was studied in two ways: firstly, by examining the distribution of clusters of neutral energy deposited in the calorimeter, and secondly, by performing a jet analysis of all the neutral and charged particles detected.

6.1 Neutral energy clusters: In the shower counters, clusters were formed by finding all counters containing at least 400 MeV of energy, and then adding to each of these cores energies of at least 100 MeV in neighbouring counters if the longitudinal positions of these energy depositions matched to within ±20 cm. Any clusters which overlapped after this procedure were merged, but not across module-to-module boundaries.

In the back arrays of lead glass a 3×3 matrix of blocks centred on each block containing at least 100 MeV was examined. Within each matrix block energies above 20 MeV were combined, and then overlapping clusters were merged. The front arrays of lead glass were clustered by first associating energy with the clusters seen in the back arrays, and then clustering any remaining energy according to the same energy criteria as for the back arrays. The glass cluster energies were corrected for angle of incidence, and for energy loss in the coil of the magnet (~ 1 RL of Al) and in ≈ 0.3 RL of iron magnetic shielding in front of the lead-glass arrays. These corrections typically amounted to about 15% of the cluster energy. A negligibly small number of events containing very large clusters in the back arrays, with little or no associated energy in the front arrays, were rejected from further consideration (again due to cosmic-ray or stray-proton interactions).

The fraction of the total neutral energy associated with clusters after this procedure remained high, but showed a slight dependence on E^0_T, increasing from 80% at 10 GeV to 95% at 30 GeV.

The two clusters with the highest transverse energies $(\varepsilon^0_T)_1$ and $(\varepsilon^0_T)_2$ were chosen from each event, and the ratio $[(\varepsilon^0_T)_1+(\varepsilon^0_T)_2]/E^0_T$ formed. The mean value of this fraction within each E^0_T bin is shown as a function of E^0_T in fig. 5. The rise to a value above 0.85 has already been used as evidence for the dominance of two-jet events at high transverse energy [1]. The mean value of the ratio $(\varepsilon^0_T)_1/E^0_T$, also shown in fig. 5, shows that this rise is not due to one-cluster dominance, although the ratio does rise above 0.5.

This two-cluster structure cannot be due to π^0 pairs since their production rate at $\sqrt{s}$ = 62 GeV is a factor of about 10^{-3} of that for these events [8]. Also a cluster due to a single π^0 would be expected to have an angular size of about 1.5 shower counters in azimuth, whereas the mean number of counters per cluster in these data increases almost linearly from 2.7 to 3.8 over the E^0_T range covered (corresponding to a range of mean cluster energies from about 3 to 12 GeV).

6.2 Jet analysis: For performing a two-jet analysis of the data the unclustered neutral energies were again used, in order to minimize effects due to differences in the energy clustering algorithms for the shower counters and lead glass. Momentum vectors were obtained for each hit counter and each charged track as described in section 4. The jet-finding algorithm enforced a partition of the particles in each event into two spatial hemispheres, with the vectorial sum of the momenta lying within each hemisphere defining a "jet" momentum vector. An iterative technique was used, choosing the initial split into hemispheres along the normal to the largest momentum neutral particle; the normal to the larger of the two momentum sums within the hemispheres defined the next split. This procedure was repeated until the change in the larger momentum sum from successive iterations was negligibly small. This usually took only two or three iterations; a small number of events which had not converged after ten iterations were discarded. The jet axes found are close to those obtained from an analysis in which the thrust is maximized in one hemisphere. All particles in the same hemisphere as the larger of the momentum sums were assigned to that jet. The remaining particles determined the opposite jet. These jet directions were not forced to be 180° apart, but as the distribution of the difference in azimuthal angle between the jet axes shows, e.g. fig. 6 for E^0_T in the range 26—30 GeV, the back-to-back nature of the jets is clear. This correlation becomes tighter as E^0_T increases, once the effects due to the energy resolution of the detector, which also lead to an apparent tightening of the correlation, have been removed.

Confirmation of the increasing dominance of jet structure as E^0_T increases was obtained by examining the behaviour of the transverse momenta of the particles relative to the jet axes. A sphericity variable, S, was used: for each event $S = S_1 + S_2$, where $S_n = 3\Sigma j_{Ti}^2/2\Sigma p_i^2$; n = 1,2 labelled the two axes in the event, p_i was the magnitude of the momentum of particle i, j_{Ti} its transverse component relative to its jet axis, and the sums were over all particles, charged and neutral, associated with axis n. Typical distributions of S in four different E^0_T bins are shown in figs. 7a—d. The shift in the distribution towards lower S as E^0_T increases can also be seen in fig. 8, in which the mean value of S is shown as a function of E^0_T. This behaviour means that Σj_T^2 does not increase as rapidly as Σp^2 as E^0_T increases, or, equivalently, that the transverse momentum relative to the jet axes is limited other than by kinematics alone. This effect will be further investigated in section 7.

The actual values of $\langle S \rangle$ are not directly comparable with sphericity values in e^+e^- jets owing to effects arising from the granularity of our detector. The same trend is seen if the neutral energies are clustered before obtaining momentum vectors. Identical values of $\langle S \rangle$ at each E^0_T are obtained if the jet axes are determined by diagonalizing, in the jet-jet c.m., the sphericity tensor [9]: $T^{\alpha\beta} = \Sigma(\delta^{\alpha\beta} p_i^2 - p_i^\alpha p_i^\beta)$, where the sum is over all particles (index i), and α,β index the x,y,z components of the momentum vector **p**.

6.3 The deviation of the E^0_T spectrum: Since the deviation from purely exponential behaviour of the E^0_T spectrum occurs at around 20 GeV, as discussed in section 4, and it is in this region that jet behaviour becomes clearly visible, the E^0_T spectrum for those events of high sphericity only was obtained. A cut on the sphericity was chosen, using only those events for which the sphericity was 0.2 or greater (see fig. 7). Figure 9 shows this high sphericity E^0_T spectrum, together with an exponential fit over the whole E^0_T range which has a slope of ≈ -0.91. The deviation from exponential above 20 GeV seen in fig. 3 is now greatly reduced, showing that this deviation is due to low sphericity (jet-like) events.

7. JET FRAGMENTATION

To enhance the two-jet component of the data only events with a large fraction of the total neutral transverse energy contained in the two largest neutral transverse energy clusters were used. In the notation of section 6.1, events satisfying $[(\varepsilon^0_T)_1 + (\varepsilon^0_T)_2]/E^0_T \geq 0.7$ were selected. Figure 10 shows the fraction of events satisfying this requirement at each value of E^0_T. The fraction rises rapidly above E^0_T of 20 GeV. Over 75% of the data above E^0_T of 25 GeV were selected.

For more detailed studies of these jets only the charged particles within an event were used, since the separation of individual particles is straightforward and the angular resolution is better than in the neutral case. The polar angle distributions, and the transverse momenta, of the charged particles relative to the jet axes were examined. The charge ratios within the jets were also studied. Figure 11 shows the notation for some of the parameters used, and the geometrical relationships between them.

7.1 Charged cones: Distributions of $dn/d\theta_j$, where θ_j is the angle between the jet axis and the particle momentum, are shown in fig. 12, for nine bins in the p_T of the charged particles, from 0.3 GeV/c to $\geq$ 5 GeV/c. The peak at θ_j values below 45° becomes more pronounced as p_T increases, and the high θ_j background has almost disappeared for $p_T \geq 2$ GeV/c (fig. 12f). Thus the higher p_T charged particles are tightly associated with the jet direction, lying in a cone about the jet axis of half-angle $\approx$ 30°. This cone gradually shrinks as p_T increases. Figure 12i is directly comparable with the analogous distribution presented by the UA1 Collaboration for $\sqrt{s}$ = 540 GeV in $\bar{p}p$ collisions [10]. The distributions are very similar although significantly tighter in the $\sqrt{s}$ = 62 GeV regime of our data. Similar cones are observed with the neutral particles or clusters, but the granularity of the detector then tends to produce cones of artificially small half-angle. The jet cones are also quite similar to those shown by the TASSO Collaboration [11] for jet fragmentation in e^+e^- collisions, for charged-particle momenta above about 1 GeV/c.

In an attempt to model the shape of the distributions in the regions outside the cone, the charged particles within each event were randomized by generating a random ϕ and rapidity y for each particle according to the actual overall pp c.m. ϕ and y charged-particle distributions, while maintaining the magnitudes of the momenta at their real values. This procedure was expected to destroy any correlation between the original jet direction and the charged particles. The events were again analysed into two jets (although in general these directions are controlled by the unchanged neutral particles). The corresponding $dn/d\theta_j$ distributions for the randomized charged particles were normalized to the original distributions by the ratio of the averages over the regions between θ_j of 44° and 84°. These distributions are shown as smooth dashed curves in fig. 12. Evidently the shape of the distributions at high θ_j is closely modelled by the randomized events. Integrating over p_T and subtracting the normalized random distribution from the real distribution gives fig. 13, in which the 30° cone emerges clearly. The high θ_j component of the distributions is presumably largely due to spectator particles unassociated with the primary hard parton-parton interaction.

7.2 Definition of the jet: To avoid possible systematic effects arising from trigger bias and apparatus acceptance only jets for which an entire cone, of half-angle $\alpha°$ centred on the jet axis, lay inside the geometrical acceptance of the electromagnetic calorimeter were considered. The drift-chamber acceptance for charged particles effectively encompassed this neutral acceptance region. Each event could then contribute two, one, or zero jets for further study. Cone sizes of $\alpha = 15°$ and $30°$ were used at different stages of the analysis. The jet 4-momentum was recalculated considering only those charged and neutral particles with momenta lying within the cone of half-angle α about the original jet momentum vector. In particular, the jet energy, E_{jet}, was calculated as the total energy of all charged and neutral particles within the jet cone. When using a $15°$ cone, E_{jet} was corrected by a small amount (typically $\lesssim 10\%$) to compensate for not accepting the full $30°$ jet cone. Using $30°$ cones, there were about 1900 events with E°_{T} above 18 GeV, giving about 2200 well-contained jets. The conventional fragmentation variable for hadronic jets, $z = p_{\parallel}/E_{jet}$, was defined where $p_{\parallel} = \mathbf{p}.\mathbf{j}$ is the longitudinal component of the charged-particle momentum $\mathbf{p}$ along the unit 3-momentum of the jet $\mathbf{j}$, and E_{jet} is the jet energy. To ensure that only well-reconstructed tracks, with well-determined properties, were used, further cuts were made on the track quality. The results presented in the following sections did not change significantly if these cuts were removed.

7.3 Charge ratios within jets: The ratio of the number of particles with positive charge to the number with negative charge in a jet is expected to depend on the type of fragmenting parton. It is expected to be equal to 1.0 for gluon jets, to be greater than 1.0 for u quark jets, and to be less than 1.0 for d quark jets. Since there are twice as many valence u quarks as valence d quarks in the proton, the charge ratio in pp collisions is expected to be greater than one. This ratio is shown as a function of θ_j in fig. 14, for events with sphericities in the range 0 to 0.1. There is an excess of positive over negative particles close to the jet direction ($\theta_j \cong 0°$), with the ratio gradually decreasing to one at $90°$ to the jet (the spectator region). This is consistent with the expectation that these jets arise predominantly from quark, rather than gluon, fragmentation.

In most schemes of fragmentation which have been proposed, the sign of the charge of the leading charged particle (that with highest $p_{\parallel}$) in a jet is directly related to the charge of the primary fragmenting parton. The ratio R of the number of positive to the number of negative leading charged particles in the detected jets was studied in terms of the fragmentation variable z. In order to maximize the number of jets available for this study, and to reduce the effects of spectator particles on the ratios, a cone size of half-angle $15°$ was used. The ratio R is shown as a function of z in fig. 15, for E_{jet} in the range 8—25 GeV. Each jet contributes at most one particle to the numerator or deno-

minator, and only particles of $p_T \geq 1$ GeV/c were considered as reasonably associated with the hard scatter. The results obtained using a 30° cone, or no cone at all, do not change significantly from those in fig. 15. The evident trend is for R to increase from 1 as z increases. This confirms that these jets arise predominantly from u quarks, and that high z tracks are more likely to reflect the charge of the scattered quark.

The resolution in z, Δz, is complicated as a function of z, since E_{jet} contains contributions from charged and neutral particles (with different measurement resolutions) in differing fractions. Over the E_{jet} range 5—25 GeV the resolution Δz is estimated to be always $\lesssim 15\%$, and is typically $\approx 5\%$ for $z \approx 0.3$. This cannot account for the rise in R.

The increase in the ratio with increasing z could also arise from a small misalignment of the drift-chamber modules, which could introduce systematic differences between the measurements of the momenta of positive and negative tracks. To investigate such systematics, the mean values of p_T of positrons and electrons were compared in a sample of 63 e^+e^- events with invariant masses above that of the upsilon, detected in the apparatus over the same data-collection period as used for these data. They were $\langle p_T(e^+)\rangle = 6.19\pm0.37$ GeV/c and $\langle p_T(e^-)\rangle = 6.09\pm0.35$ GeV/c. These momenta are higher than most of the momenta used for the charge ratio measurements. Similarly a sample of reconstructed $K^0_S \rightarrow \pi^+\pi^-$ gave $\langle p_T(\pi^+)\rangle = 0.97\pm0.05$ GeV/c and $\langle p_T(\pi^-)\rangle = 0.98\pm0.06$ GeV/c. By studying the effect on the charge ratio R of shifting the observed p_T spectra of the leading charged particles in the jets, while enforcing compatibility with the ratio of these electron and pion measurements (within their errors), it was estimated that the change in R, ΔR, due to such a possible misalignment was $\Delta R/R < 0.2$. This is in all cases less than the size of the statistical errors.

For the much smaller sample of events in which both jets were fully contained within the apparatus, the correlation between the signs of the charged leaders in each jet could be studied. With a 15° cone, and $p_T \geq 1$ GeV/c, the number of events with two positive leaders was 49, that with two negative leaders was 25, and that with one positive and one negative was 62. These relative proportions were maintained using 30° cones, or no cone at all, and with or without a p_T cut of 1 GeV/c. With no cone requirement, but requiring $p_T \geq 1$ GeV/c, the numbers were (++) = 388, (--) = 197, and (+-) = 519. Since the proportions were quite stable, the variation of these correlations with the trigger threshold total electromagnetic energy was examined, without applying the jet-enhancement cut discussed at the beginning of section 7. The events containing charged particles with $p_T \geq 1$ GeV/c in each of the two opposite jet hemispheres were divided according to the signs of the charged leaders, thus obtaining three classes (++), (+-) [or (-+)], and (--). The numbers in each

class were normalized to the total number $N=(++)+(+-)+(--)$ to obtain the fractions $(++)/N$, $(+-)/N$, and $(--)/N$. These are plotted against the trigger threshold in fig. 16. It is evident that the number of $(++)$ relative to $(--)$ increases as the threshold, and correspondingly the transverse energy in the events, increases. This indicates an increasingly important contribution of jets from quark fragmentation.

7.4 Transverse momentum relative to the jet axis: For each charged particle within the 30° jet cone the transverse momentum component, j_T, perpendicular to the jet momentum vector was calculated. The data were binned in $p_{||}$ and z. Within each bin of $p_{||}$ (or z), and in each of three jet energy ranges 5—10, 10—15, and 15—25 GeV, the mean value was obtained from the distribution of j_T, and plotted in figs. 17 and 18. Both sets of curves show what has become known as the "sea-gull effect", in which j_T is constrained to be small at small $p_{||}$ and z values, and reaches a plateau as $p_{||}$ and z increase. There is little variation with E_{jet} above $z \approx 0.1$. The results were further found to be insensitive to a variation of the jet cone angle between 25° and 35° above $p_{||} \approx 2$ GeV/c or $z \approx 0.1$. Below these values the geometrical constraint of the cone angle tends to slightly reduce the j_T observed.

To show that this plateau in j_T is not due to constraints imposed by the apparatus acceptance a similar approach to that used in the $dn/d\theta_j$ distributions was followed. The charged particles in each event were replaced by the same number of Monte Carlo particles, with the same magnitudes of momenta, but with ϕ and y chosen randomly from the overall observed charged particle distributions. The j_T values were recalculated and the results compared with the original curves. A typical comparison, for j_T as a function of $p_{||}$, integrated over all $E_{jet} \geq 5$ GeV, is shown in fig. 19. The fact that the randomized values rise much more rapidly than the real ones confirms that the limited nature of the j_T is not due to acceptance effects. A similar rapid rise in the randomized event j_T is seen as a function of z, and in all three E_{jet} bands.

Above $z \approx 0.1$ these results are quite comparable to those found by the TASSO Collaboration [11] using their thrust axis results, at similar jet energies. The j_T values here are lower than those seen by the UA1 Collaboration [10] at $\sqrt{s} = 540$ GeV in $\bar{p}p$ collisions, although their jet energies (above 30 GeV) are also higher than those of this paper.

8. CONCLUSIONS

In pp interactions at $\sqrt{s}$ = 62.3 GeV two-jet structure clearly emerges at total neutral transverse energies above 20 GeV. This is seen in the deviation of the E^0_T spectrum from a pure exponential, in the rapid decrease in the event sphericity, and in the increasing dominance of the two largest clusters of electromagnetic energy deposition. The charged particles in these jets show a clear cone structure, and exhibit the expected limited transverse momentum fragmentation relative to the jet axis. The charge ratio within each jet shows that these jets are predominantly due to quarks. The correlations of the signs of the leading charged particles in the jets indicate that this quark contribution increases with increasing transverse energy.

Acknowledgements

We thank the staff and management of CERN for their assistance in the successful operation of this experiment, in particular those of the ISR and DD Divisions. We are grateful to R. Gros for his continued devotion to the maintenance of our apparatus, and to M.A. Huber for her dedicated secretarial and data-management work. We also acknowledge the assistance of A.M. Smith of the CERN EF Division. C. Baltay helped in early stages of the experiment.

REFERENCES

[1] A.L.S. Angelis et al., Phys. Lett. **126B** (1983) 132.

[2] T. Akesson et al., Phys. Lett. **128B** (1983) 354.

[3] M. Banner et al., Phys. Lett. **118B** (1982) 203;
G. Arnison et al., Phys. Lett. **123B** (1983) 115.

[4] C. De Marzo et al., Phys. Lett. **112B** (1982) 173;
C. De Marzo et al., Nucl. Phys. **B211** (1983) 375;
B. Brown et al., Phys. Rev. Lett. **49** (1982) 711.

[5] J.S. Beale et al., Nucl. Instrum. Methods **117** (1974) 501.

[6] M. Morpurgo, Cryogenics **17** (1977) 89;
L. Camilleri et al., Nucl. Instrum. Methods **156** (1978) 275.

[7] P. Bagnaia et al., Z. Phys. **C20** (1983) 117;
P. Bagnaia et al., Measurement of very large transverse momentum jet production at the CERN $\bar{p}p$ collider, preprint CERN EP/84-12, submitted to Phys. Lett.

[8] A.L.S. Angelis et al., Nucl. Phys. **B209** (1982) 284.

[9] J. D. Bjorken and S. J. Brodsky, Phys. Rev. **D1** (1970) 1416.

[10] G. Arnison et al., Phys. Lett. **132B** (1983) 214;
G. Arnison et al., Phys. Lett. **132B** (1983) 223.

[11] M. Althoff et al., Jet production and fragmentation in e^+e^- annihilation at 12—43 GeV, preprint DESY 83-130, submitted to Z. Phys. C.

FIGURE CAPTIONS

Fig. 1: The apparatus viewed along the beam axes.

Fig. 2: The pp c.m. acceptance of the electromagnetic calorimeter, in y (rapidity) and ϕ.

Fig. 3: The spectrum events/integrated luminosity as a function of E^0_T at $\sqrt{s}$ = 62.3 GeV.

Fig. 4: a) The mean ratio of charged to neutral transverse energy as a function of E^0_T;
b) The mean charged transverse energy as a function of E^0_T.

Fig. 5: The mean fraction of neutral transverse energy contained in the two most energetic clusters (closed circles), and the mean fraction of neutral transverse energy contained in the most energetic cluster (open circles), as a function of E^0_T.

Fig. 6: The azimuthal angle between the two jet axes defined in the text for events with E^0_T in the range 26—30 GeV.

Fig. 7: Distributions of the sphericity variable S defined in the text; (a)—(d) are for E^0_T ranges 10—12 GeV, 16—18 GeV, 19—20 GeV, and 26—30 GeV, respectively.

Fig. 8: The mean value of sphericity S as a function of E^0_T.

Fig. 9: The spectrum events/integrated luminosity as a function of E^0_T at $\sqrt{s}$ = 62.3 GeV, for events of sphericity $S \geq 0.2$ only.

Fig. 10: The fraction of events at each E^0_T in which at least 70% of the neutral transverse energy is contained in the two most energetic neutral clusters.

Fig. 11: Relation between the jet unit 3-momentum j, and a charged-particle momentum vector p, showing θ_j, j_T, and $p_{\parallel}$.

Fig. 12: Distributions of the polar angle θ_j between the jet direction and the charged particles within the same hemisphere, for nine bins of p_T of the particles: (a) 0.3—0.5, (b) 0.5—0.7, (c) 0.7—1.0, (d) 1.0—1.5, (e) 1.5—2.0, (f) 2.0—3.0, (g) 3.0—4.0, (h) 4.0—5.0, and (i) $\geq$ 5.0 GeV/c. The dashed curves are those from randomized events (see text).

Fig. 13: The distribution of θ_j resulting from using the randomized events to estimate the background in the real events, for $p_T \geq 0.3$ GeV/c (see text).

Fig. 14: The charge ratio of the number of positive to number of negative charged particles as a function of the polar angle θ_j relative to the jet axis, for events with sphericities in the range 0 to 0.1.

Fig. 15: Charge ratio of leading charged particles in jets, as a function of the fragmentation variable z. Errors are statistical only.

Fig. 16: Charged leader (with $p_T \geq 1$ GeV/c) sign correlations in opposite hemispheres. Closed circles denote the fraction (++)/all, open circles (--)/all, and crosses (+-)/all.

Fig. 17: The mean transverse momentum relative to the jet axis, j_T, of charged particles as a function of the longitudinal momentum along the jet axis, $p_{\parallel}$, in three bands of jet energy E_{jet}: (a) 5—10, (b) 10—15, (c) 15—25 GeV.

Fig. 18: The mean transverse momentum relative to the jet axis, j_T, of charged particles as a function of $z = p_{\parallel}/E_{jet}$, in three bands of jet energy E_{jet}: (a) 5—10, (b) 10—15, (c) 15—25 GeV.

Fig. 19: j_T as a function of $p_{\parallel}$ for charged particles, for all $E_{jet} \geq 5$ GeV. The closed circles are for real data, and the open circles for randomized data (see text).

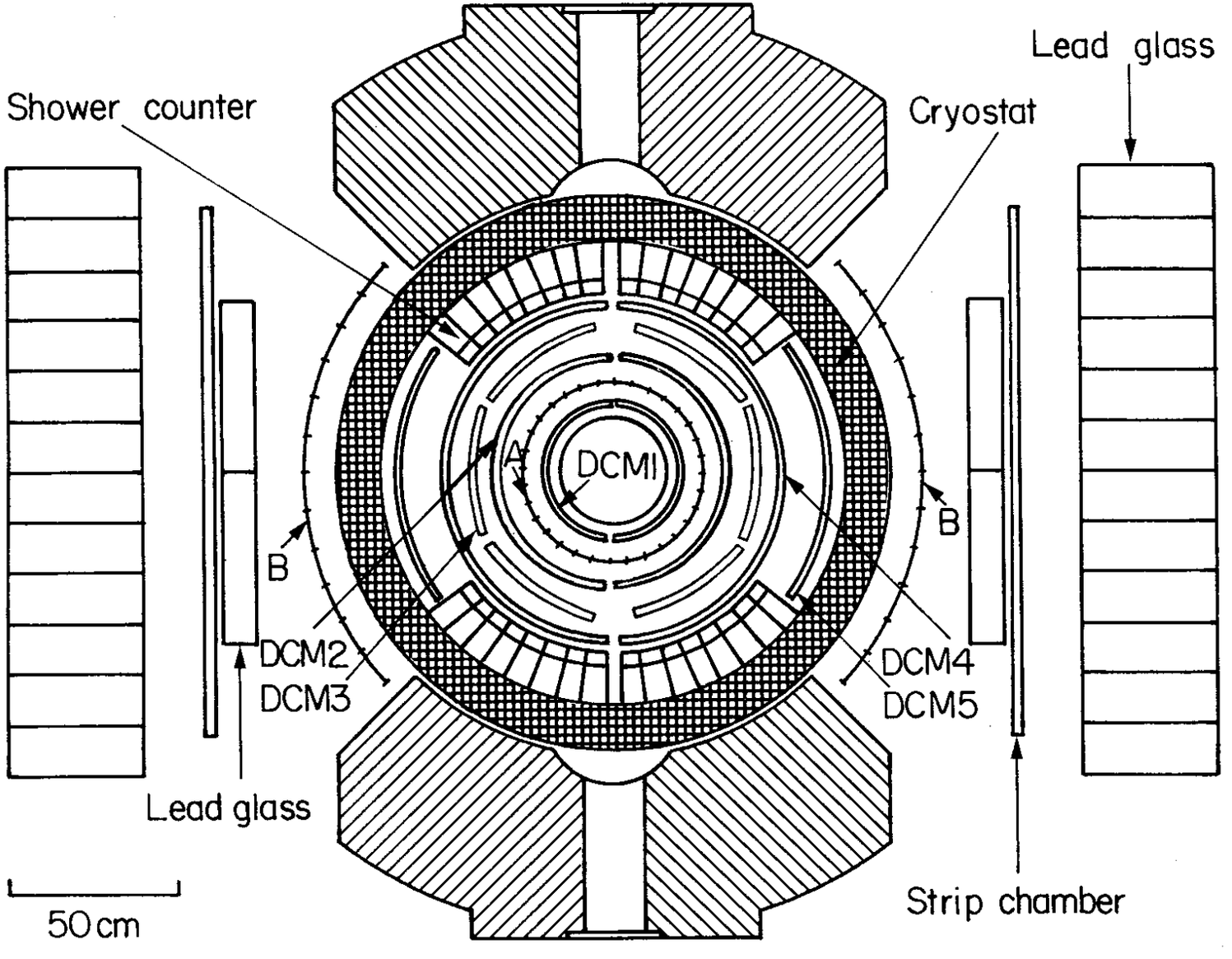
Lead glass
Shower counter
Cryostat
A
DCM1
B
B
DCM2
DCM3
DCM4
DCM5
Lead glass
50 cm
Strip chamber

Fig. 1

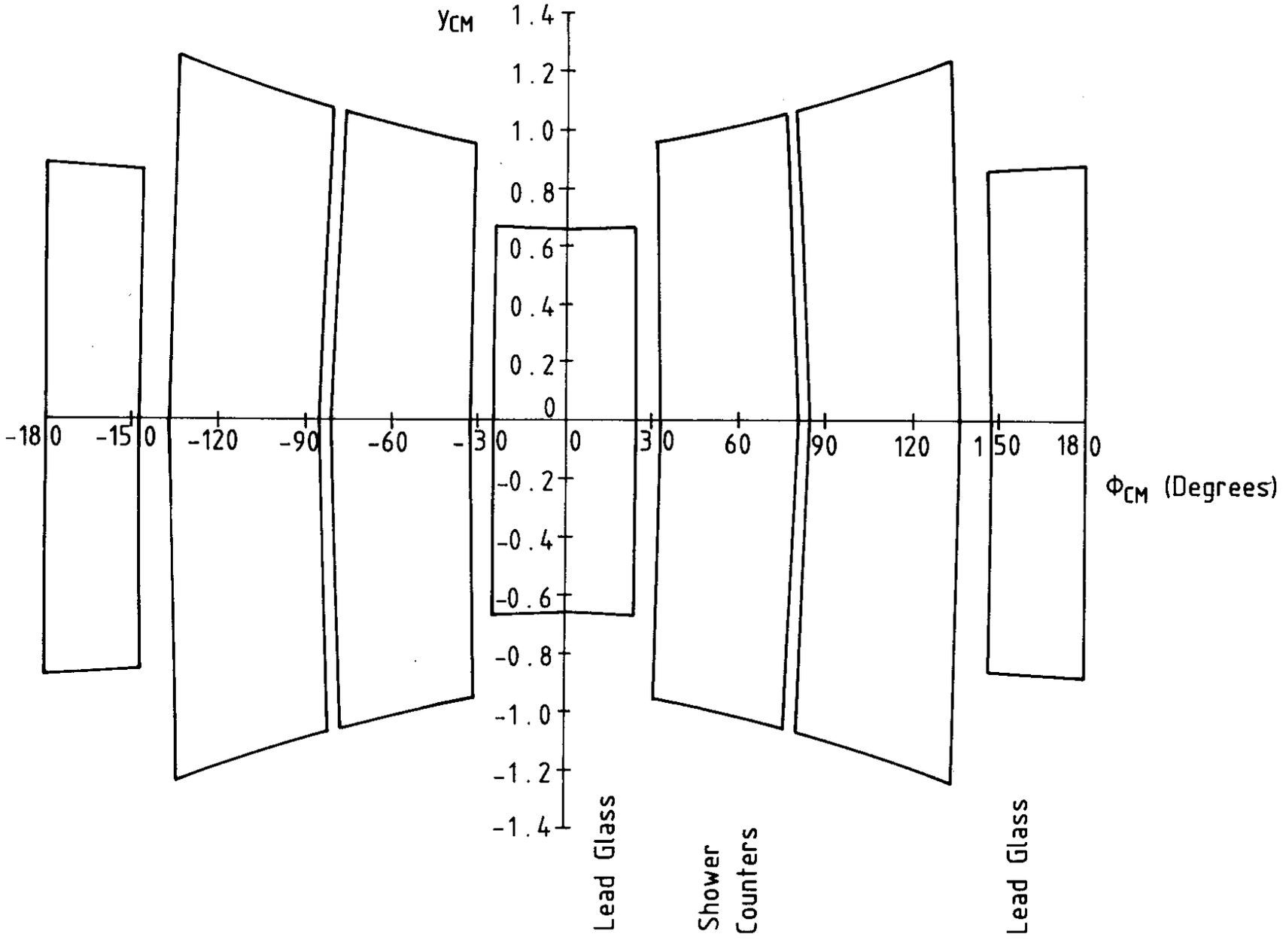
y_{CM}
1.4
1.2
1.0
0.8
0.6
0.4
0.2
0
-0.2
-0.4
-0.6
-0.8
-1.0
-1.2
-1.4
-180
-150
-120
-90
-60
-30
0
30
60
90
120
150
180
Φ_{CM} (Degrees)
Lead Glass
Shower Counters
Lead Glass

Fig. 2

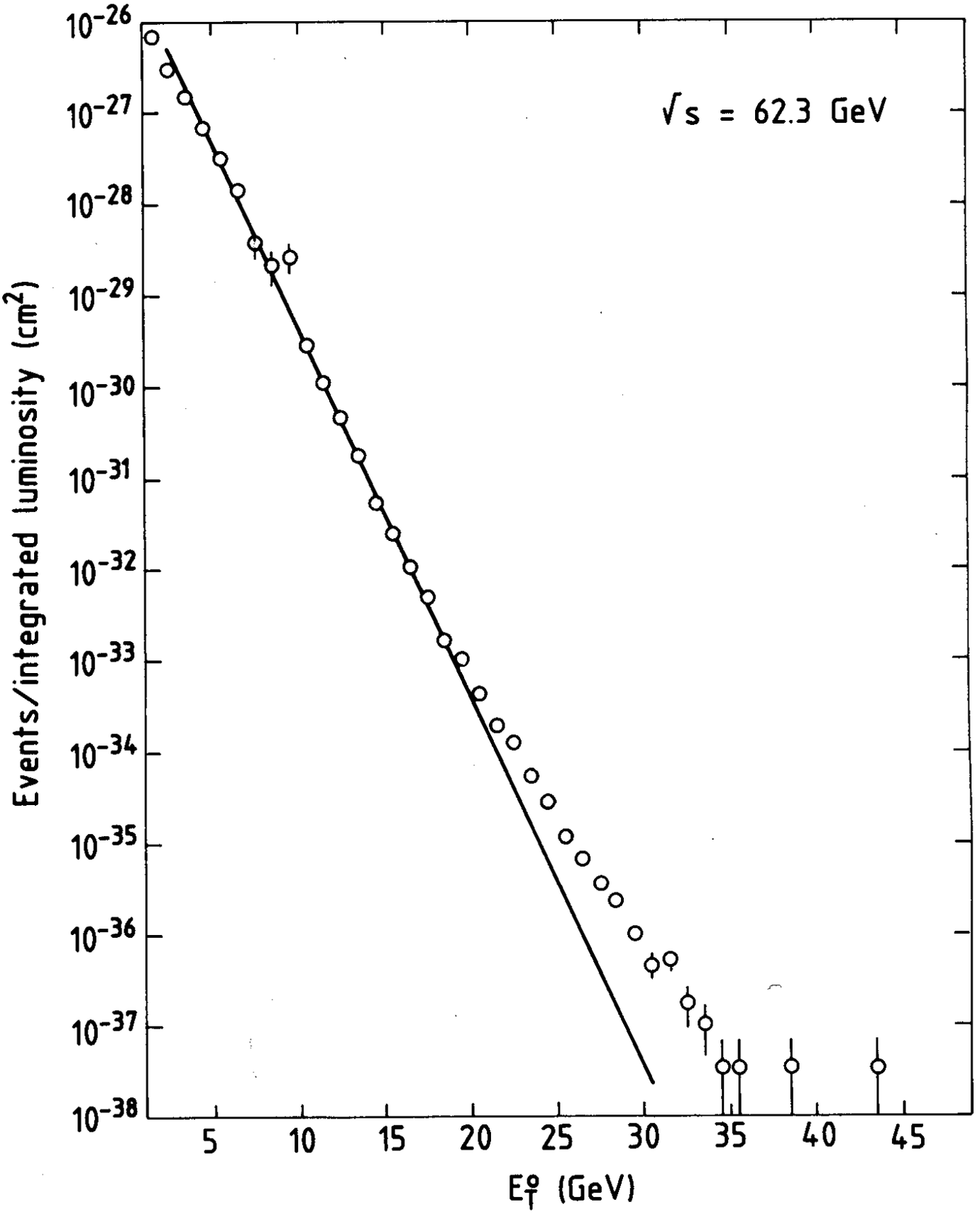
√s = 62.3 GeV
Events/integrated luminosity (cm²)
10⁻²⁶
10⁻²⁷
10⁻²⁸
10⁻²⁹
10⁻³⁰
10⁻³¹
10⁻³²
10⁻³³
10⁻³⁴
10⁻³⁵
10⁻³⁶
10⁻³⁷
10⁻³⁸
5
10
15
20
25
30
35
40
45
E$_T^0$ (GeV)

Fig. 3

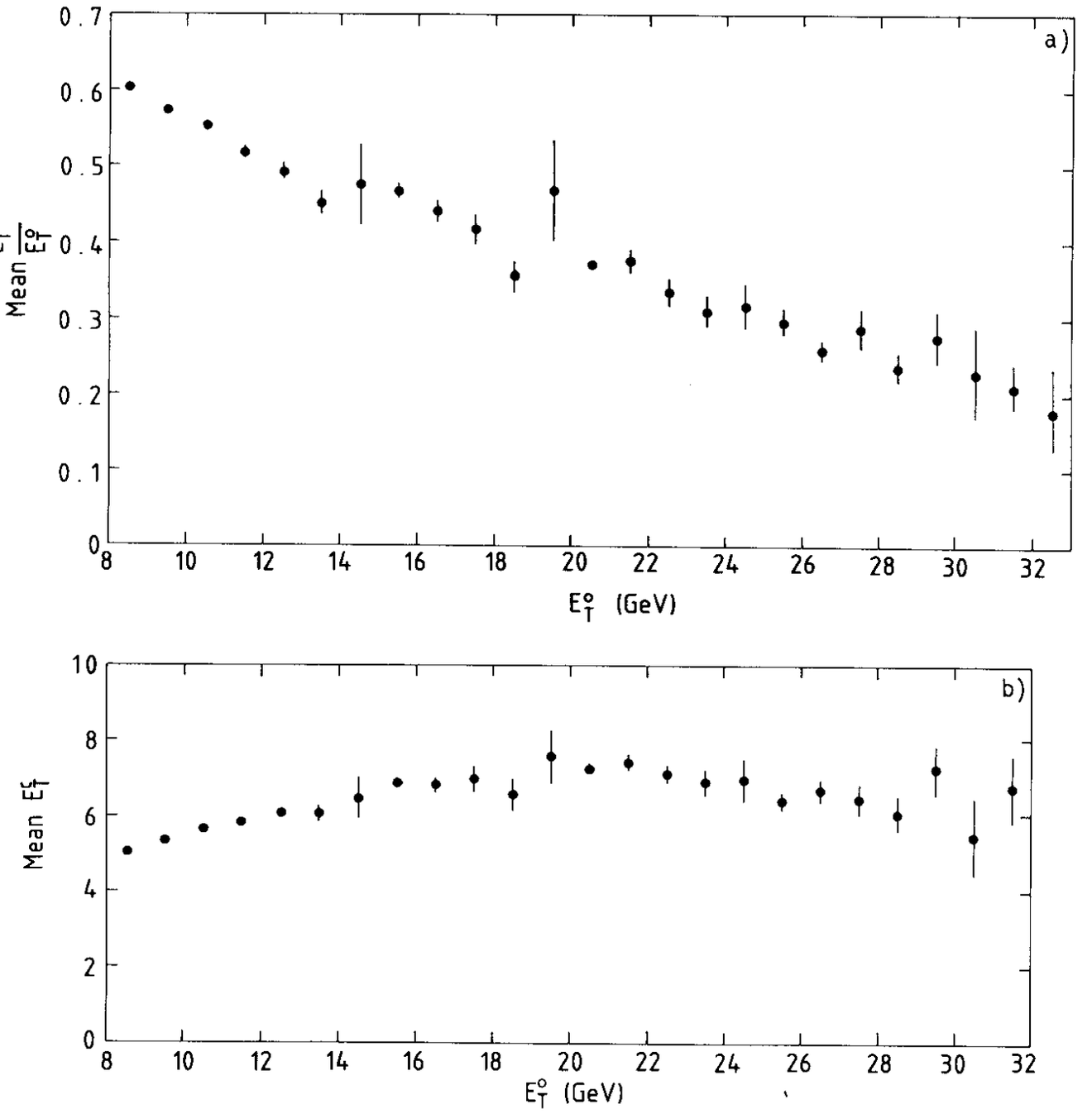
a)
Mean $\frac{E_T^c}{E_T^o}$
0.7
0.6
0.5
0.4
0.3
0.2
0.1
0
8
10
12
14
16
18
20
22
24
26
28
30
32
E_T^o (GeV)
b)
Mean E_T^c
10
8
6
4
2
0
8
10
12
14
16
18
20
22
24
26
28
30
32
E_T^o (GeV)

Fig. 4

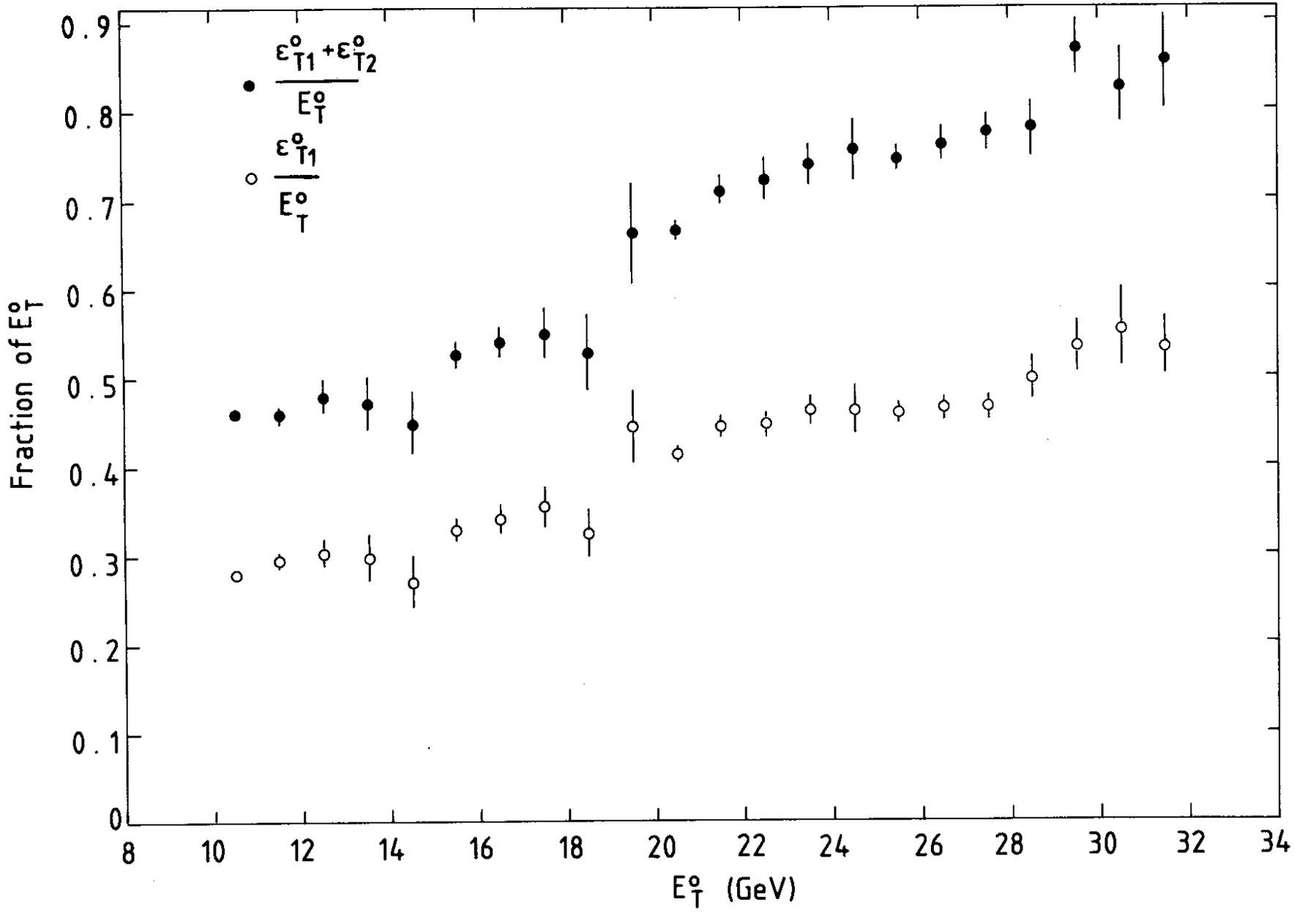
0.9
0.8
0.7
0.6
0.5
0.4
0.3
0.2
0.1
0
Fraction of E_T^o
$\frac{\varepsilon_{T1}^o + \varepsilon_{T2}^o}{E_T^o}$
$\frac{\varepsilon_{T1}^o}{E_T^o}$
8
10
12
14
16
18
20
22
24
26
28
30
32
34
E_T^o (GeV)

Fig. 5

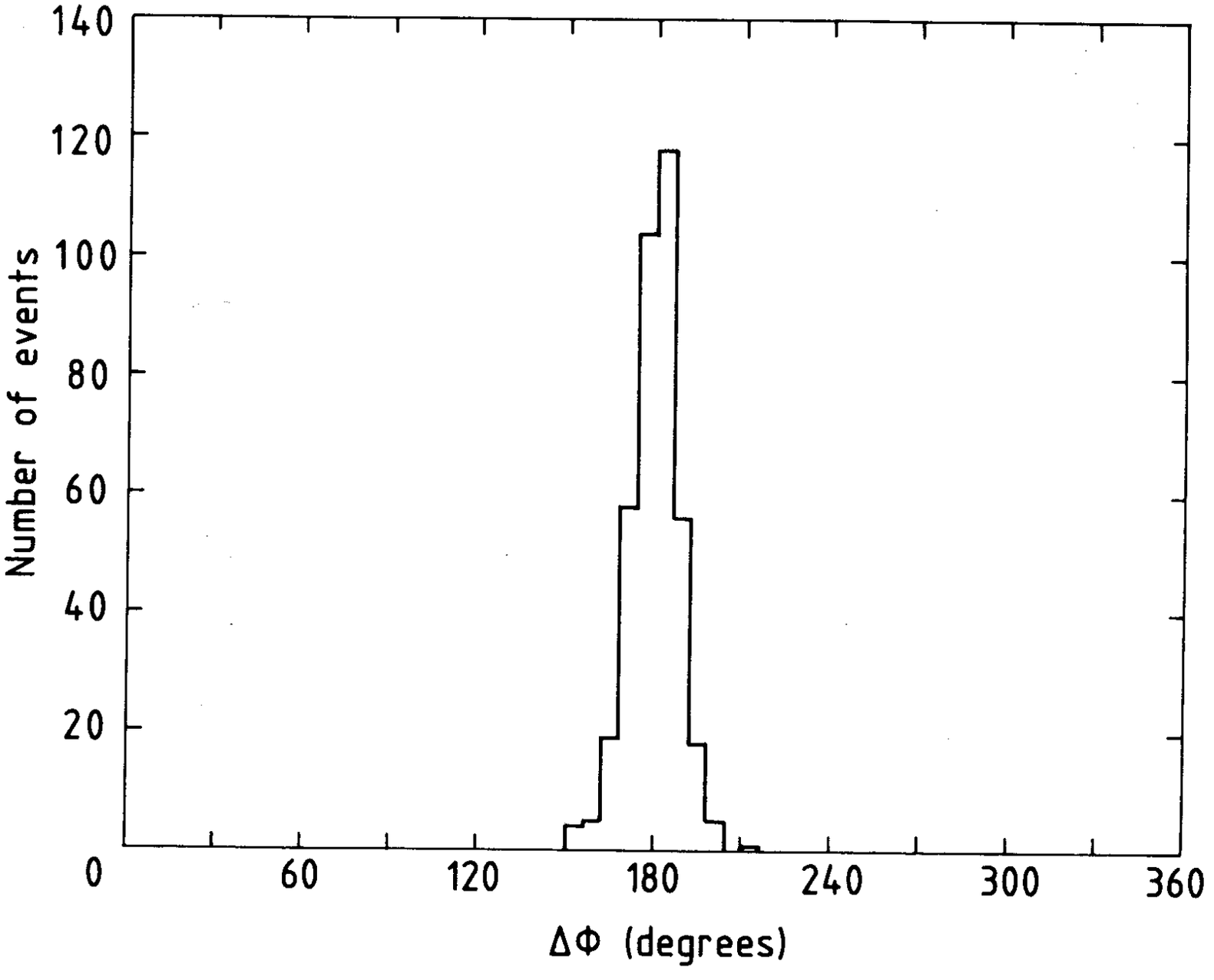
140
120
100
80
60
40
20
0
Number of events
60
120
180
240
300
360
ΔΦ (degrees)

Fig. 6

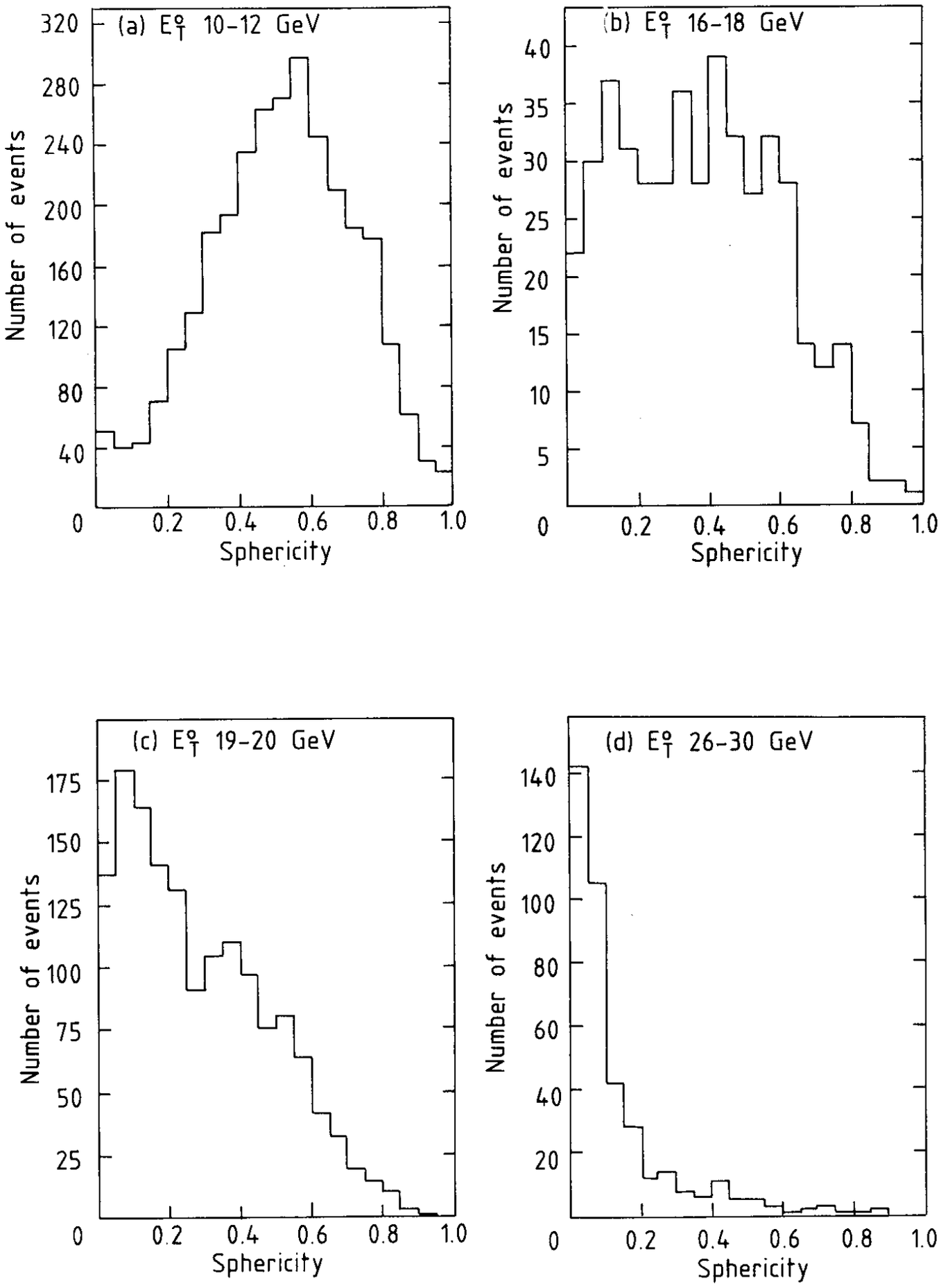
(a) E_T^o 10-12 GeV
(b) E_T^o 16-18 GeV
(c) E_T^o 19-20 GeV
(d) E_T^o 26-30 GeV
Number of events
Sphericity
0
0.2
0.4
0.6
0.8
1.0
320
280
240
200
160
120
80
40
35
30
25
20
15
10
5
175
150
125
100
75
50
25
140
120
100
80
60
40
20

Fig. 7

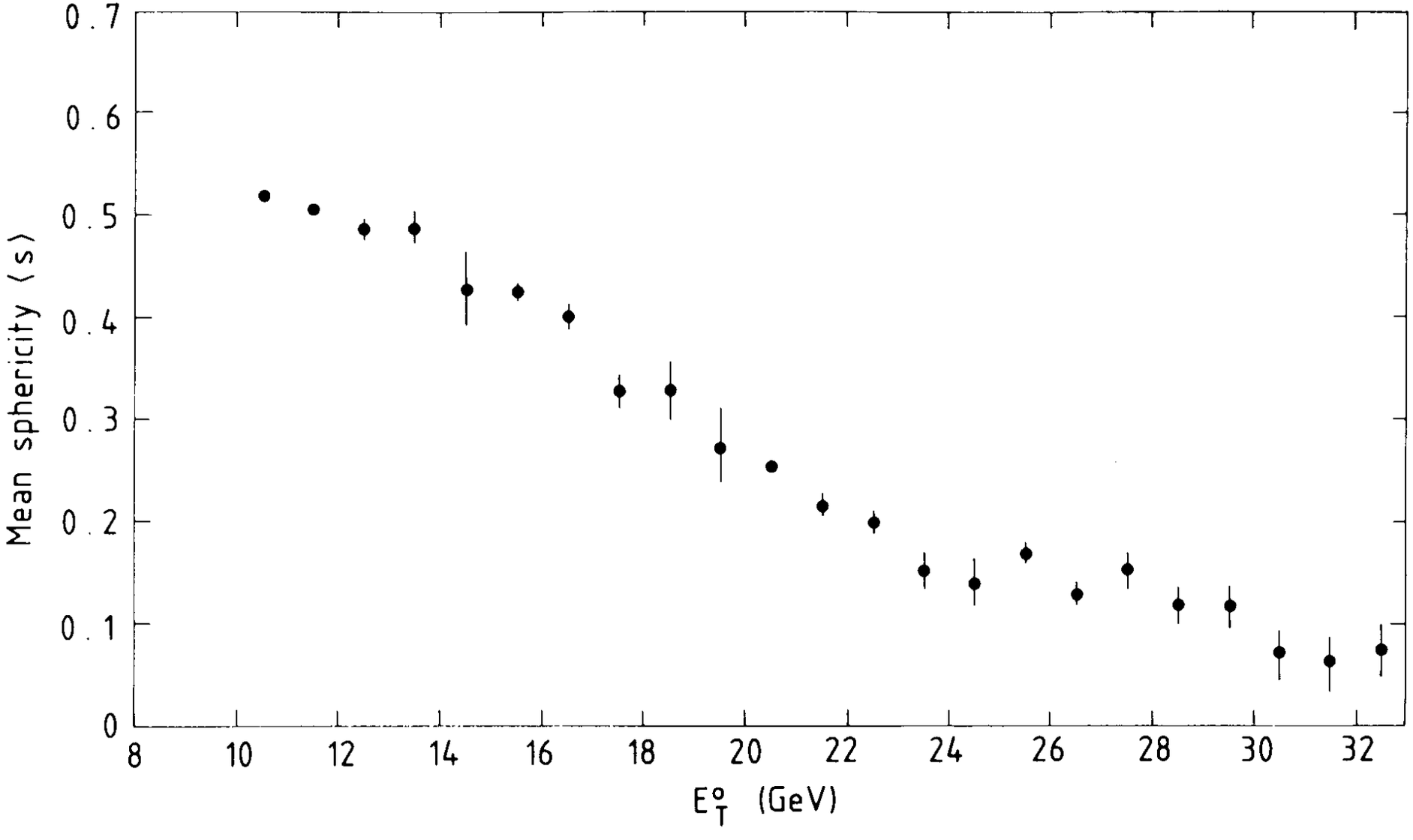
0.7
0.6
0.5
0.4
0.3
0.2
0.1
0
Mean sphericity ⟨s⟩
8
10
12
14
16
18
20
22
24
26
28
30
32
E_T^o (GeV)

Fig. 8

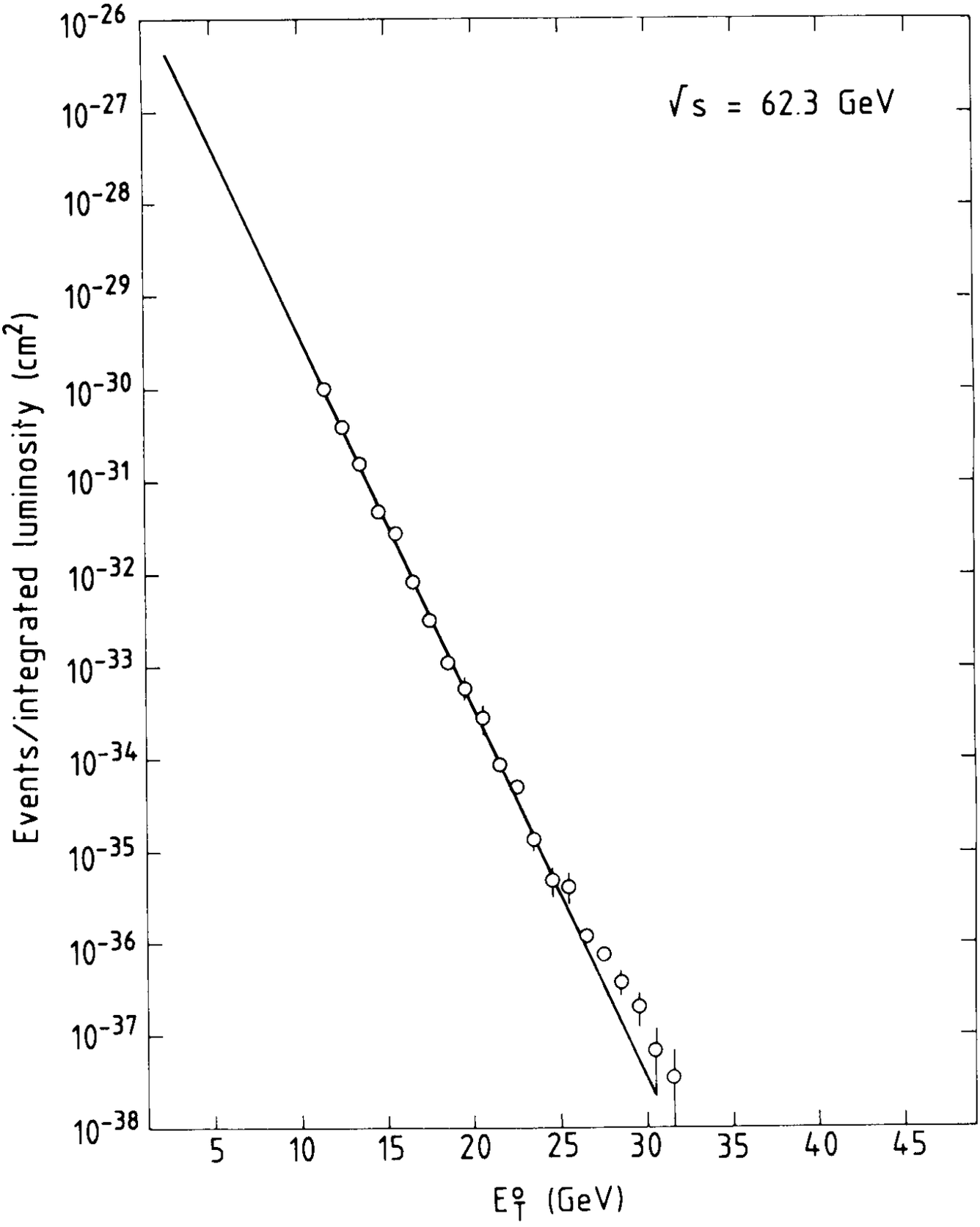
√s = 62.3 GeV
Events/integrated luminosity (cm²)
10⁻²⁶
10⁻²⁷
10⁻²⁸
10⁻²⁹
10⁻³⁰
10⁻³¹
10⁻³²
10⁻³³
10⁻³⁴
10⁻³⁵
10⁻³⁶
10⁻³⁷
10⁻³⁸
5
10
15
20
25
30
35
40
45
E°T (GeV)

Fig. 9

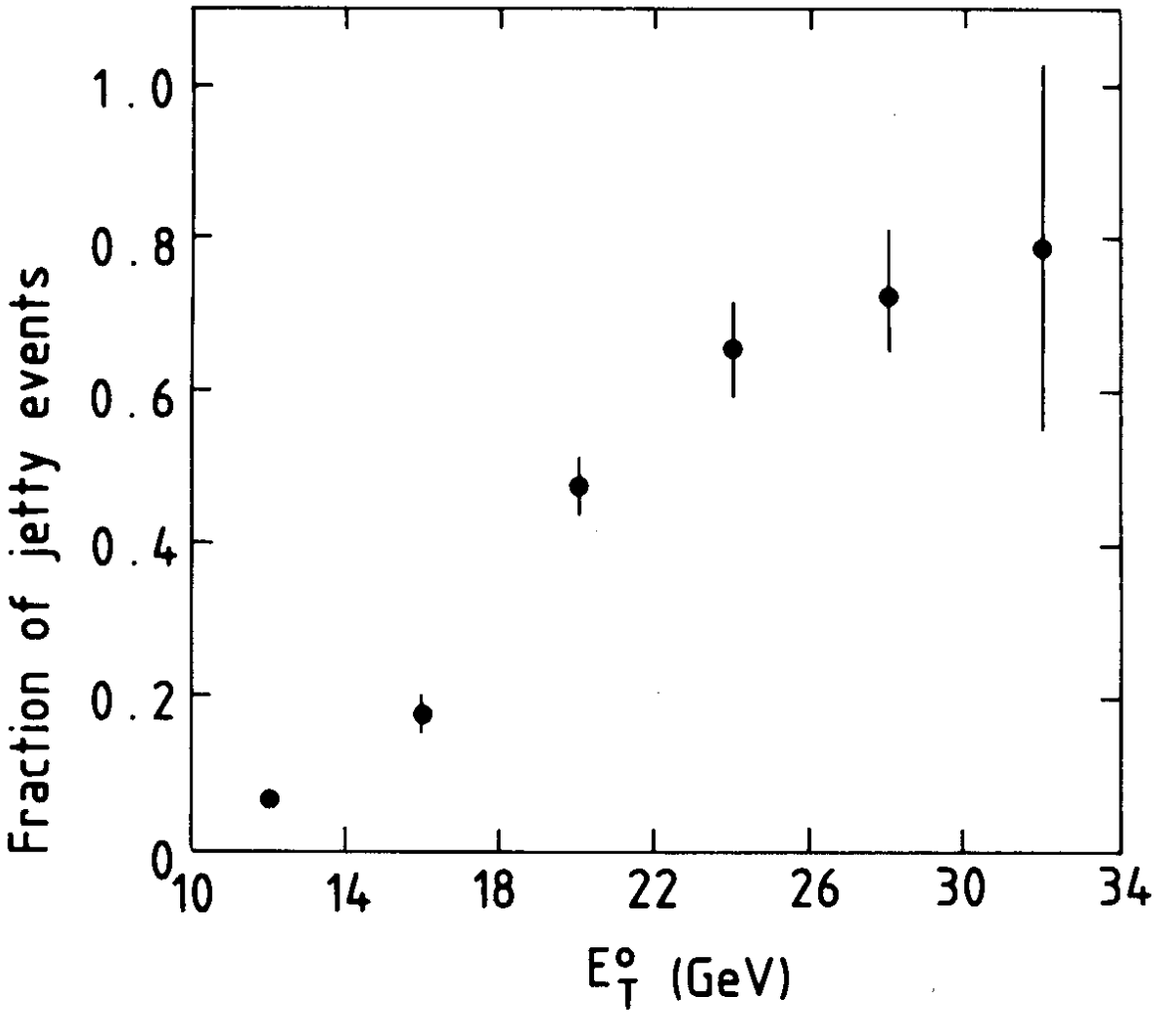
Fraction of jetty events
1.0
0.8
0.6
0.4
0.2
0
10
14
18
22
26
30
34
E_T^o (GeV)

Fig. 10

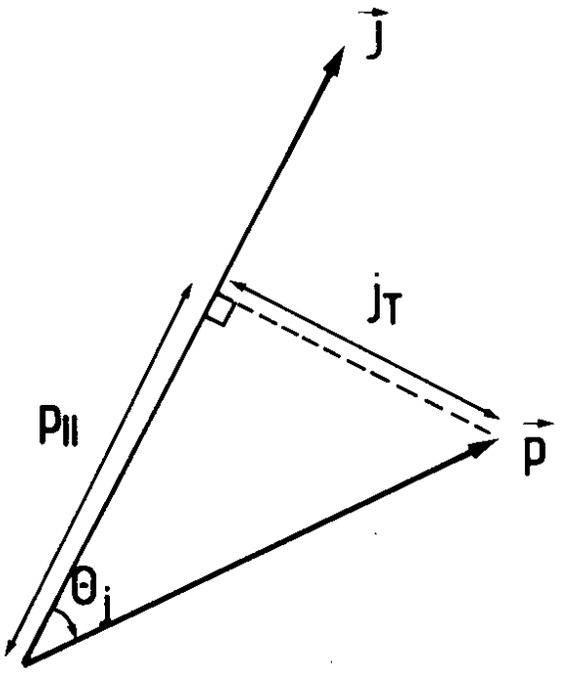
$\vec{J}$
j_T
p_{II}
$\vec{p}$
Θ_j

Fig. 11

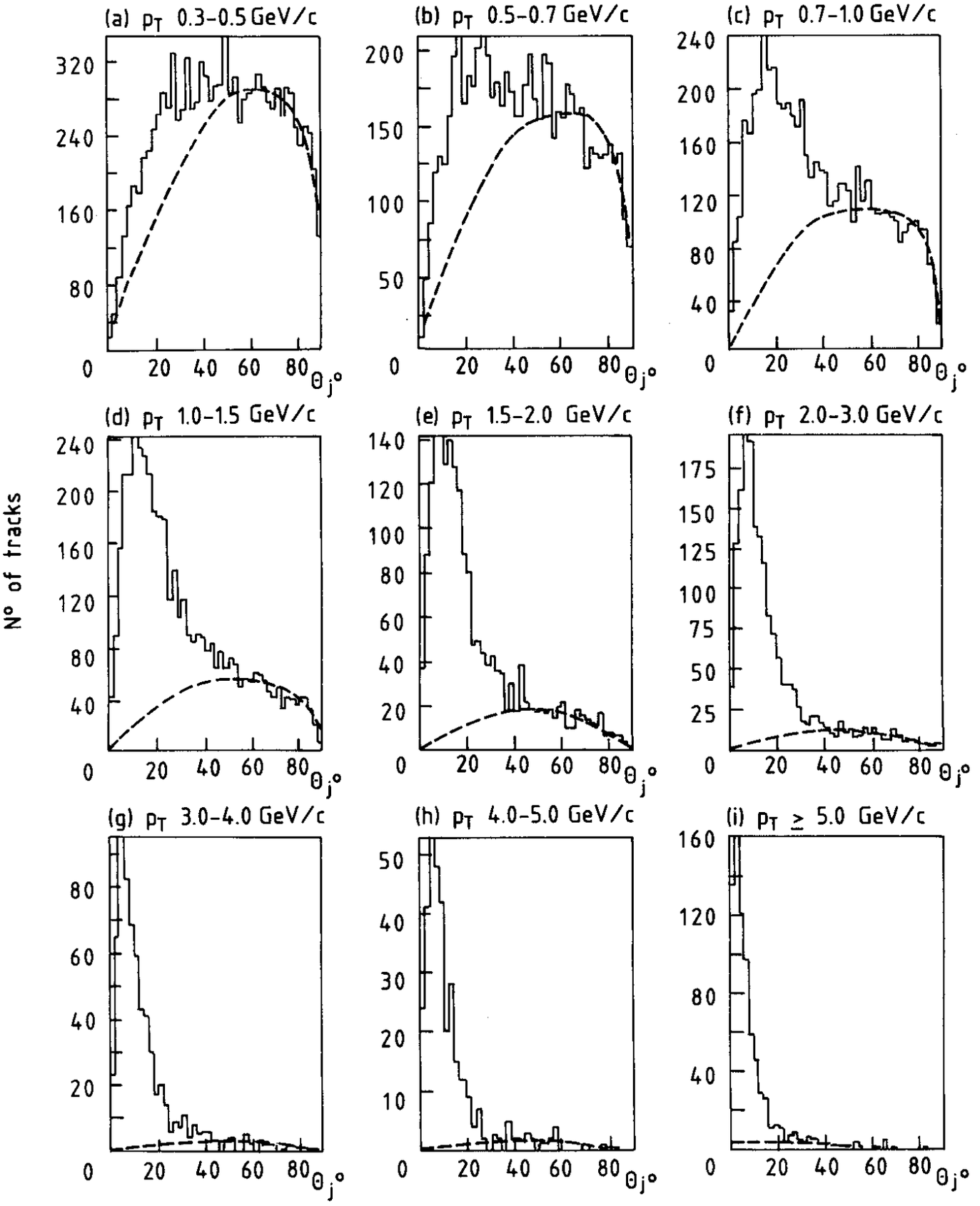
(a) p_T 0.3–0.5 GeV/c
(b) p_T 0.5–0.7 GeV/c
(c) p_T 0.7–1.0 GeV/c
(d) p_T 1.0–1.5 GeV/c
(e) p_T 1.5–2.0 GeV/c
(f) p_T 2.0–3.0 GeV/c
(g) p_T 3.0–4.0 GeV/c
(h) p_T 4.0–5.0 GeV/c
(i) $p_T \geq$ 5.0 GeV/c
N° of tracks
θ_j°

Fig. 12

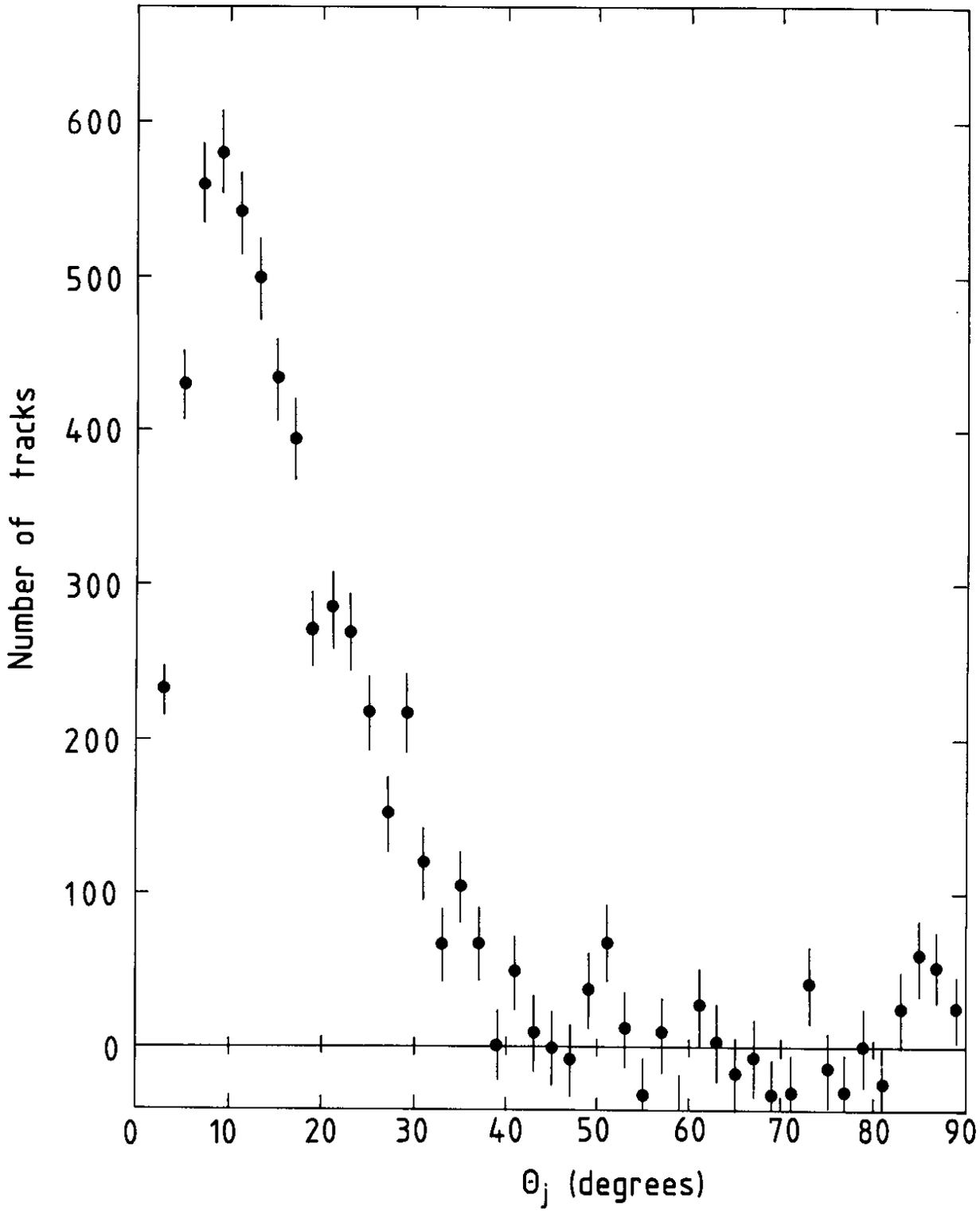
Number of tracks
600
500
400
300
200
100
0
0
10
20
30
40
50
60
70
80
90
Θ_j (degrees)

Fig. 13

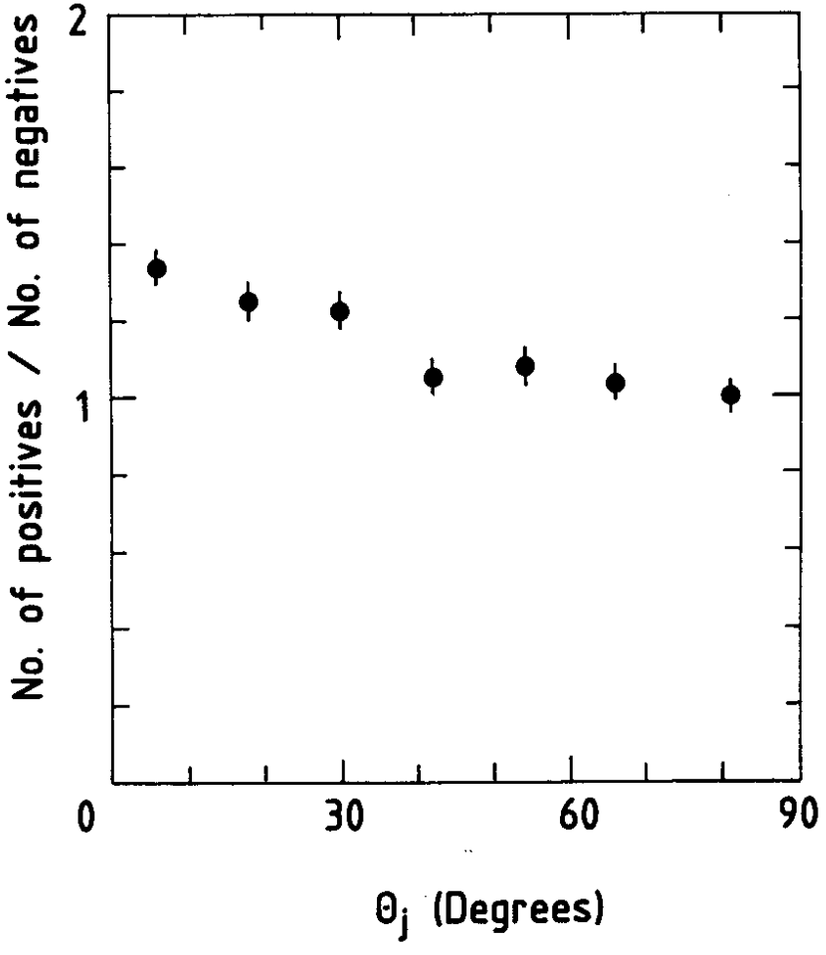
No. of positives / No. of negatives
2
1
0
30
60
90
Θ_j (Degrees)

Fig. 14

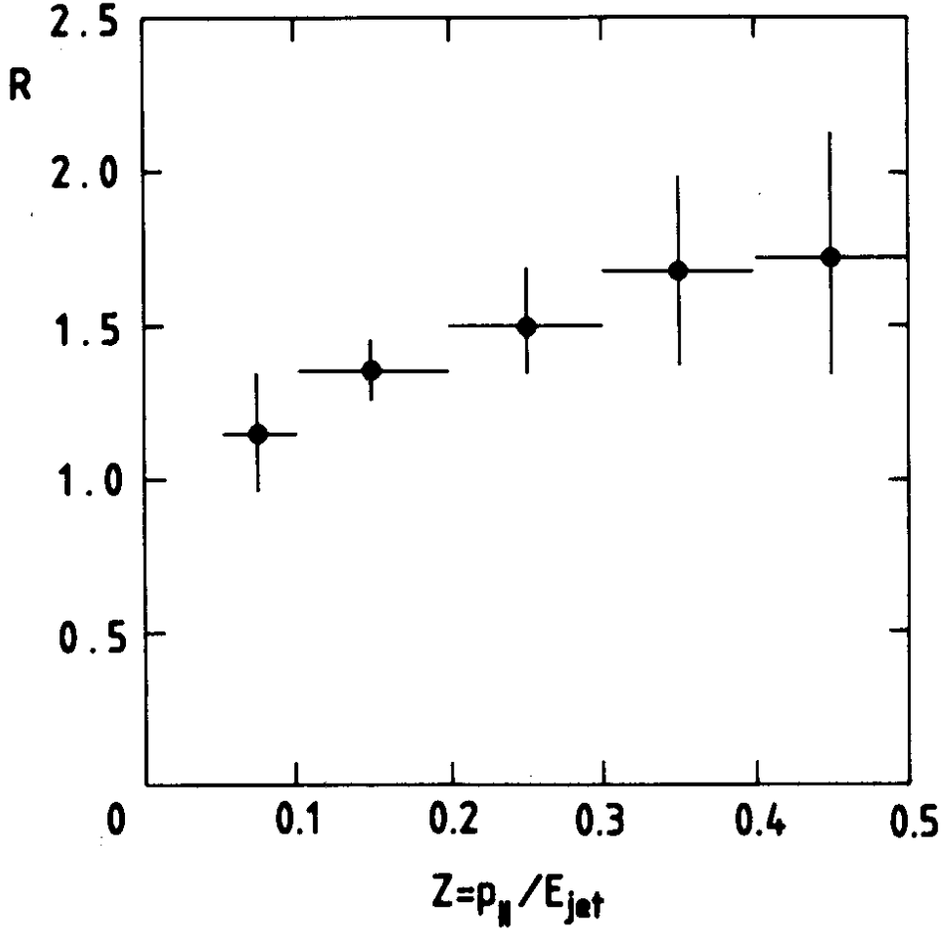
R
2.5
2.0
1.5
1.0
0.5
0
0.1
0.2
0.3
0.4
0.5
$Z=p_{\parallel}/E_{jet}$

Fig. 15

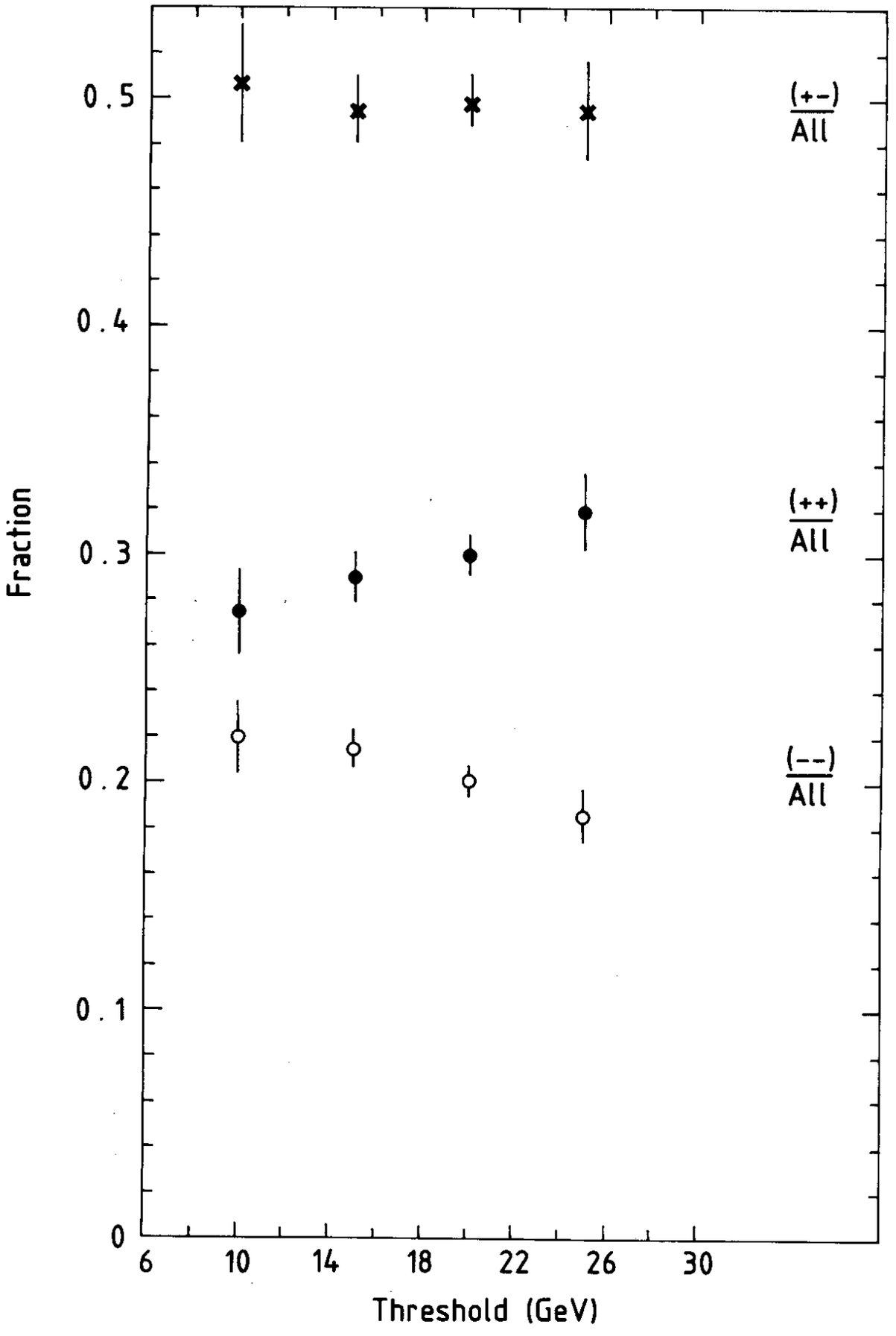
0.5
0.4
0.3
0.2
0.1
0
Fraction
6
10
14
18
22
26
30
Threshold (GeV)
(+-)
All
(++)
All
(--)
All

Fig. 16

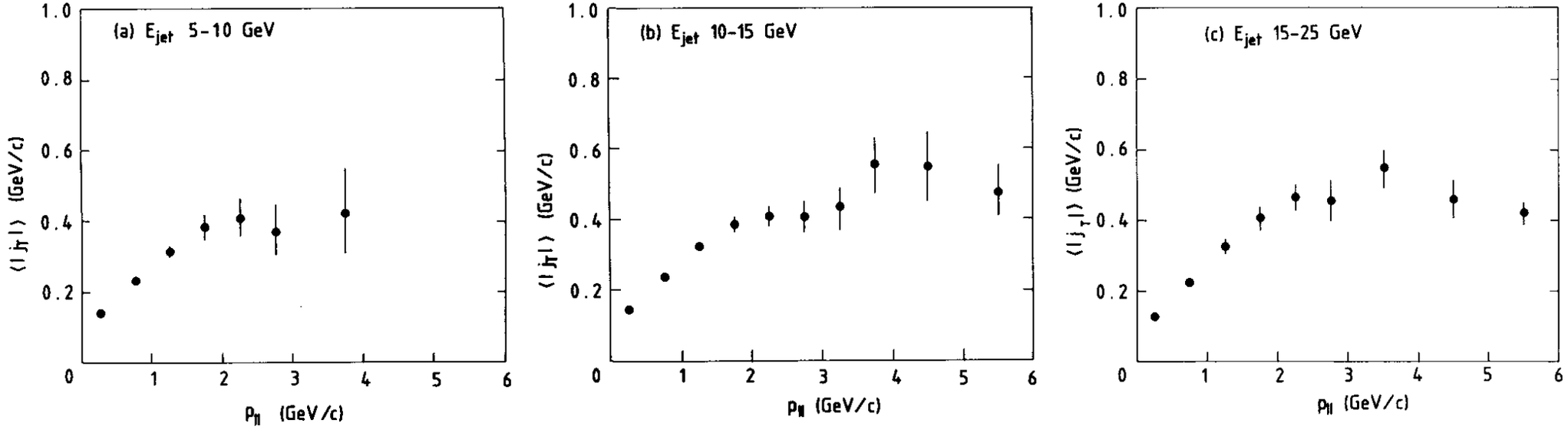
(a) E_{jet} 5-10 GeV
(b) E_{jet} 10-15 GeV
(c) E_{jet} 15-25 GeV
$\langle |j_T| \rangle$ (GeV/c)
$p_{||}$ (GeV/c)
0
0.2
0.4
0.6
0.8
1.0
1
2
3
4
5
6

Fig. 17

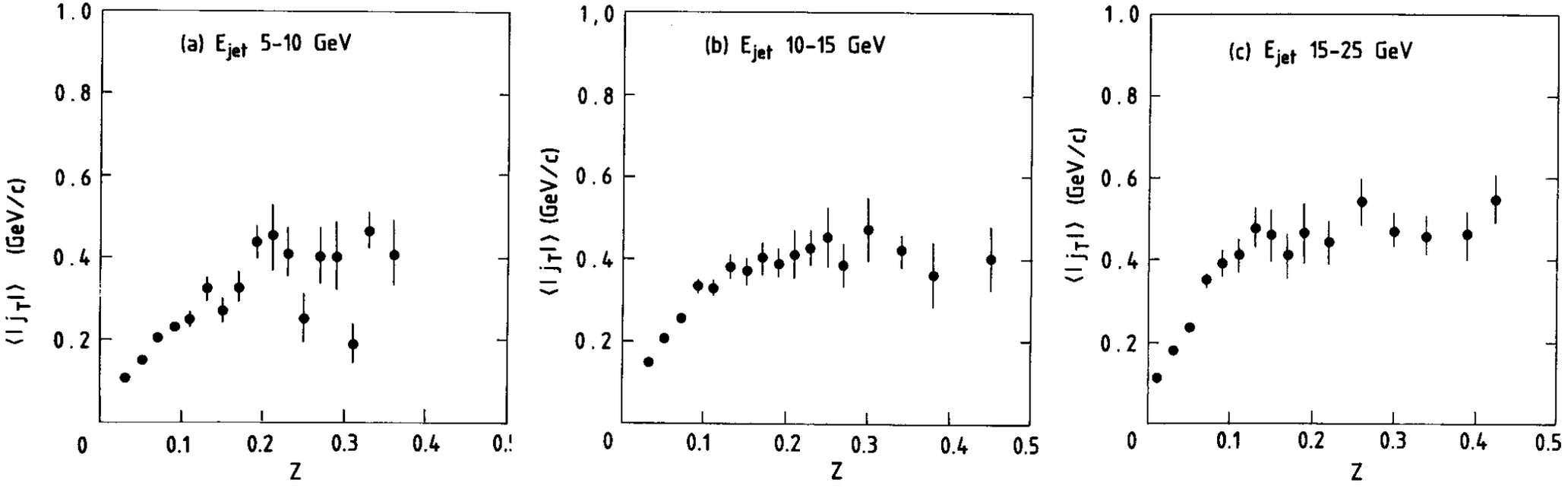
(a) E_{jet} 5-10 GeV
(b) E_{jet} 10-15 GeV
(c) E_{jet} 15-25 GeV
$\langle |j_T| \rangle$ (GeV/c)
Z
1.0
0.8
0.6
0.4
0.2
0
0.1
0.2
0.3
0.4
0.5

Fig. 18

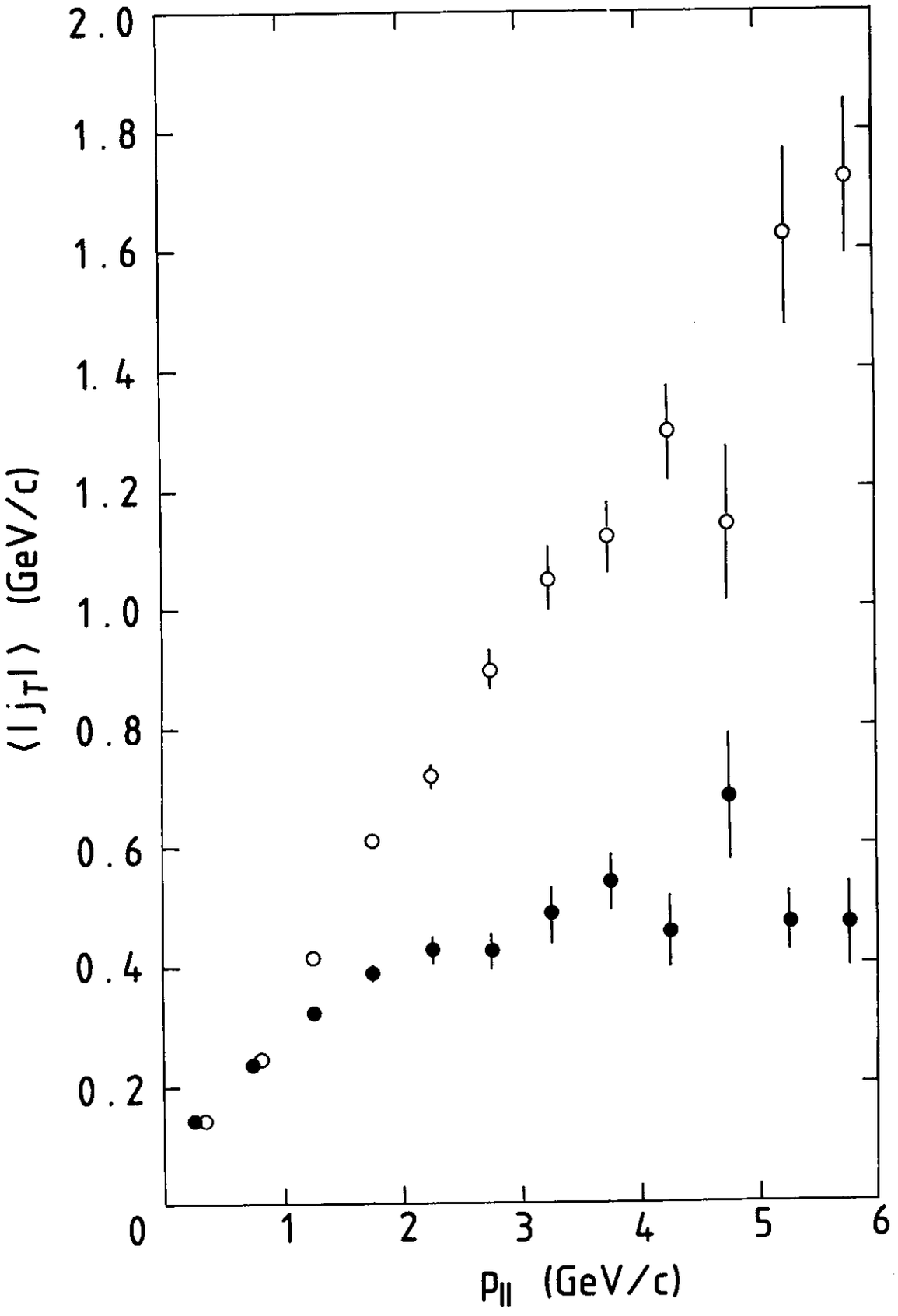

Fig. 19